ADVANCED FUNCTIONAL MATERIALS
www.afm-journal.de

A Co- and Ni-Free P2/O3 Biphasic Lithium Stabilized Layered Oxide for Sodium-Ion Batteries and its Cycling Behavior

Liangtao Yang, Juan Miguel López del Amo, Zulipiya Shadike, Seong-Min Bak, Francisco Bonilla, Montserrat Galceran, Prasant Kumar Nayak, Johannes Rolf Buchheim, Xiao-Qing Yang, Teófilo Rojo, and Philipp Adelhelm**

Cobalt- and nickel-free cathode materials are desirable for developing low-cost sodium-ion batteries (SIBs). Compared to the single P-type and O-type structures, biphasic P/O structures become a topic of interest thanks to improved performance. However, the added complexity complicates the understanding of the storage mechanism and the phase behavior is still unclear, especially over consecutive cycling. Here, the properties of biphasic P2(34%)/O3(60%) $Na_{0.8}Li_{0.2}Fe_{0.2}Mn_{0.6}O_2$ and its behavior at different states of charge/discharge are reported on. The material is composed of single phase O3 and P2/O3 biphasic particles. Sodium occupies the alkali layers, whereas lithium predominantly (95%) is located in the transition metal layer. An initial reversible capacity of 174 mAh g^{-1} is delivered with a retention of 82% dominated by Fe^{3+}/Fe^{4+} along with contributions from oxygen and partial $Mn^{3+/4+}$ redox. Cycling leads to complex phase transitions and ion migration. The biphasic nature is nevertheless preserved, with lithium acting as the structure stabilizer.

1. Introduction

Thanks to their outstanding performance, lithium-ion batteries (LIBs) are widely applied in portable electronics as well as in the rising markets of electric mobility and grid storage.[1] On the other hand, there have been concerns on whether the materials supply can follow the projected need for battery materials.[2] As a result, alternative batteries based on low cost and more abundant elements are highly studied.[3] Among different options, sodium-ion batteries (SIBs) appear very attractive. LIBs and SIBs rely on the same working principle, that is, alkali ions and electrons are reversibly stored in host structures. The cell voltages of SIBs are relatively lower than that of LIBs, but there are also some advantages. For example, aluminum can be used as current collector for SIBs which is not only cheaper than the copper but may also allow full battery discharge to 0 V which eases cell shipping. Another example is the reduced tendency of Na^+ to form antisite defects in layered oxides.[4] Overall, the development of SIBs aims at using abundant elements, such as Mn and Fe, and avoiding or minimizing the contents of scarcer elements such as Li, Co, Ni (LIBs), Pb (lead acid batteries), or rare-earth metals (Ni-MH batteries). As positive electrode materials for SIBs, layered transition metal oxides and polyanionic compounds rich in manganese and/or iron are therefore extensively studied.[5] For sodium layered oxides $Na_x[TMs]O_2$ (TMs: transitions metal(s), $0 < X \leq 1$), the most common structures are P2, P3, and O3 (nomenclature after Delmas et al.[6]). Which structure prevails largely depends on the TMs,

L. Yang, Dr. P. K. Nayak, Dr. J. R. Buchheim, Prof. P. Adelhelm
Institute of Technical Chemistry and Environmental Chemistry
Friedrich-Schiller University Jena
Jena 07743, Germany
E-mail: philipp.adelhelm@hu-berlin.de

L. Yang, Prof. P. Adelhelm
Institute of Chemistry
Humboldt-University Berlin
Brook-Taylor-Str. 2, and Helmholtz-Zentrum Berlin (HZB)
Berlin 12489, Germany

The ORCID identification number(s) for the author(s) of this article can be found under https://doi.org/10.1002/adfm.202003364.

© 2020 The Authors. Published by Wiley-VCH GmbH. This is an open access article under the terms of the Creative Commons Attribution-NonCommercial License, which permits use, distribution and reproduction in any medium, provided the original work is properly cited and is not used for commercial purposes.

DOI: 10.1002/adfm.202003364

Dr. J. M. L. del Amo, Dr. F. Bonilla, Dr. M. Galceran, Prof. T. Rojo
Centro de Investigación Cooperativa de Energías Alternativas
(CIC energiGUNE)
Basque Research and Technology Alliance (BRTA)
Parque Tenológico de Alava
Vitoria-Gasteiz 01510, Spain
E-mail: teo.rojo@ehu.eus

Dr. Z. Shadike, Dr. S.-M. Bak, Dr. X.-Q. Yang
Chemistry Division
Brookhaven National Laboratory
Upton, NY 11973, USA

Dr. S.-M. Bak
National Synchrotron Light Source II
Brookhaven National Laboratory
Upton, NY 11973, USA

Prof. T. Rojo
Department of Inorganic Chemistry Faculty of Science and Technology
University of the Basque Country
Bilbao 48080, Spain

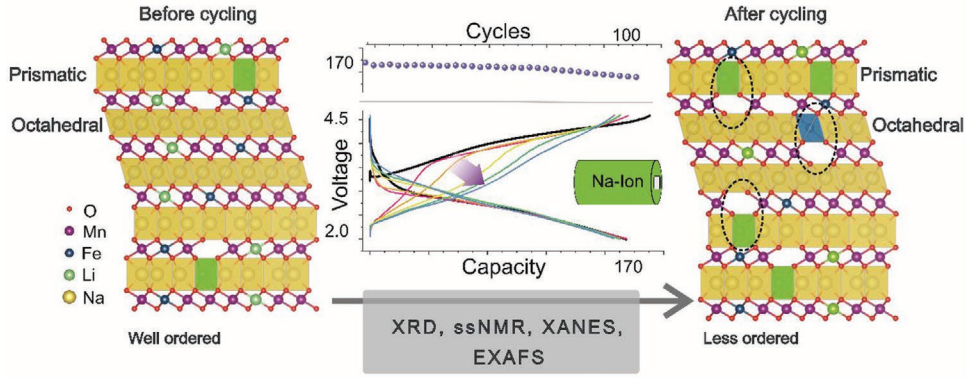

Scheme 1. Illustration of the crystal structure before and after cycling, capacity retention, voltage profiles, and used analytical tools.

the sodium content x and the synthesis conditions.[7] In case of Mn-containing materials, Jahn–Teller distortion by Mn^{3+}[8] causes even more structural complexity[9] typically leading to fast capacity fading and voltage decay.[10] In general, phase transitions during cycling are undesired and hence partial substitution of the TMs by structure stabilizing elements is an important strategy for improving electrode performance. For example, the Komaba group[11] reported on P2-type $Na_{2/3}Fe_{0.5}Mn_{0.5}O_2$ with an initial capacity of 190 mAh g^{-1} originating from TM^{3+}/TM^{4+} (TM=Mn, Fe) redox. Above 3.8 V, a OP4 phase (alternate stacking of O2 and P2 layers) forms which is detrimental for achieving long cycle life.[12] To overcome this issue, partial substitution with, for example, Ni or Mg has been employed.[13] A series of Ni substituted $Na_{0.67}[Mn_{0.5+y}Ni_yFe_{0.5-2y}]O_2$ (y =0, 0.1, 0.15) materials has been studied by operando XRD. The results indicated that Fe substitution by Ni delays the phase transition during charging by reducing the concentration of Fe^{4+}.[13a]

An interesting substitutional element (dopant) is lithium, which allows aliovalent substitution of transition metals (due to its similar ionic radius) as well as isovalent substitution of sodium.[14] It has been shown for different layered oxides that the addition of lithium on TM sites can suppress the Jahn–Teller effect and can delay phase transformation at high voltages thereby improving cycle life.[15] For example, Lufeng et al. also reported on $Na_{0.66}Li_{0.18}Fe_{0.12}Mn_{0.7}O_2$ with a lithium stabilized structure, resulting in a capacity retention of 87% after 80 cycles.[16] The overall understanding, however, is still poor and further studies are needed to clarify the role of Li as additive in such structures and its lattice occupation during cycling.

Another recent approach for achieving better electrode performance is the use of P2/O3 composite structures. Guo et al. reported on P2/O3-$Na_{0.66}Li_{0.18}Mn_{0.71}Ni_{0.21}Co_{0.08}O_2$ with a ratio of 94:6 (wt%, P2:O3), which delivered a specific capacity about 200 mAh g^{-1} cycled between 1.5–4.5 V.[17] Keller et al. reported a specific capacity of 155 mAh g^{-1} for $Na_{0.76}Mn_{0.5}Ni_{0.3}Fe_{0.1}Mg_{0.1}O_2$ with 41 wt% of P2 + P3 phase and 49 wt% of O3 when cycled at 15 mA g^{-1} in the potential range of 2.0–4.3 V.[18] The Rojo group prepared a P2-O3 composite by solid-state synthesis with the composition $Na_{2/3}Li_{0.18}Fe_{0.2}Mn_{0.8}O_2$ (O3 phase being the minor fraction, which exhibited about 125–140 mAh g^{-1} during the first cycles (1.5–4.2 V) with moderate cycle life.[19] Notably, the material did not contain any Ni or Co. Recently, Ganesh et al. reported on $Na_{0.5}Li_{0.1}[Fe0.5Mn0.5]_{0.9}O_2$ with a capacity retention of 92.5% only after 30 cycles.[20] Although this approach seems promising, cycle life, voltage, and capacity need further improvement. Even more importantly, the electrode processes during cycling need to be better understood.

Following up on this concept, we here report on a P2/O3 biphasic material with the composition $Na_{0.8}Li_{0.2}Fe_{0.2}Mn_{0.6}O_2$. Different from the previous approach, we synthesized the material by sol-gel method and shift the voltage window to higher values (2.0–4.6 V) to lift the average redox potential for increasing energy density. This synthesis approach leads to a P2/O3 composite which is rich in O3 phase (60%). A range of different structure analysis methods were used to characterize the material before and during cycling. Structural properties were determined by X-ray powder diffraction (XRD), oxidation states were studied by X-ray photoelectron spectroscopy (XPS). Scanning electron microscopy (SEM) and transmission electron microscopy (TEM) were applied to study the particle morphology as well as the nanoscopic properties. Solid-State Nuclear magnetic resonance (ssNMR) spectroscopy was used to determine the Li^+ occupation during cycling. X-ray absorption spectroscopy (XAS) was used to determine the transition metal and oxygen valence states. The very good reversibility of the electrode reaction was shown by galvanostatic cycling between 2.0–4.6 V versus Na^+/Na for over 100 cycles. The material exhibited a specific capacity of 174 mAh g^{-1} in the initial cycles when tested in half cells (versus sodium). Overall, the present approach leads to a significant improvement with respect to capacity, cycle life, and average redox potential compared to state-of-the art. The content of the study is sketched in **Scheme 1**, illustrating the main relevant aspects.

2. Results

2.1. Structural Properties

The diffraction pattern of the synthesized $Na_{0.8}Li_{0.2}Fe_{0.2}Mn_{0.6}O_2$ ($Na_{0.81}Li_{0.20}Fe_{0.19}Mn_{0.61}O_2$ by ICP analysis) material shows the presence of a composite composed of P2 and O3 layered structures/domains, as illustrated in **Figure 1**. The experimental and calculated XRD patterns agree well with the hexagonal crystal

© 2020 The Authors. Published by Wiley-VCH GmbH

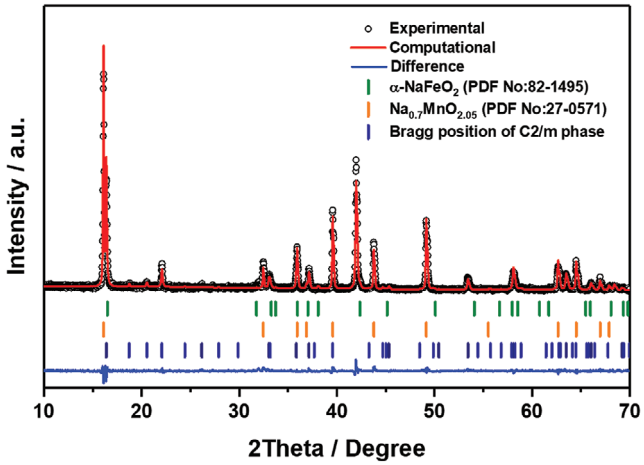

Figure 1. XRD pattern of $Na_{0.8}Li_{0.2}Fe_{0.2}Mn_{0.6}O_2$. Experimental data (black dots) and results from Rietveld refinement (red line) are shown. The Rietveld refinement was carried out with space groups P63/mmc (orange bar), $R\bar{3}m$ (green bar), and C2/m (blue bar).

system with space group $P6_3/mmc$ ($Na_{0.7}MnO_2$-type, JCPDS 27-0571) and the trigonal-rhombohedral system with space group $R\bar{3}m$ (α-$NaFeO_2$, JCPDS 82-1495). This is in line with previous studies on $Na_xMn_{1-y}Fe_yO_2$ ($0.5 < x < 1.0$, $y = 1/3, 1/2, 2/3$) for which both types of phases (P2 and O3) have been reported.[6,21] Oxides with P2 structure crystallize in the hexagonal system with space group $P6_3/mmc$ in which the alkali metal has a trigonal prismatic coordination. Compounds with O3 structure crystallize in the trigonal-rhombohedral system with space group $R\bar{3}m$ in which the coordination of the alkali metal is octahedral.

Rietveld refinement was used to determine the unit cell parameters of both P2 and O3 phases as well as their amounts, see Table S1, Supporting Information. The material was rich in O3 phase with 60 wt% compared to 34 wt% for P2. The reflexes between 2θ = 20–30° are indexed as a secondary phase with $C2/m$ symmetry (Li_2MnO_3, JCPDS 27-1252 and α-$NaMnO_2$-O'3-type JCPDS 72-0830). On the other hand, they may also be the result of transition metal ion and Li ion ordering within the metal oxide, which is a well reported phenomenon in layered oxides with partial lithium accommodated in TM-O_2 layers.[22] However, it is difficult to relate this ordering to either the P2/O3 sodium biphasic particles or only the $C2/m$ secondary phase.

The morphology of the material was characterized by SEM (Figure S1, Supporting Information). The material consists of ill-defined agglomerates with several µm in size which are composed of fused crystallites with a facetted, plate-like structure typically between 0.5 and 4 µm in size. The biphasic nature is not visible by SEM, which is because of the similarity of both structures. The oxidation states of the transition metals were studied by XPS, see Figure S2, Supporting Information. All spectra were calibrated with the binding energy of C 1s (284.8 eV). Next to the satellite peaks, the Mn 2p spectrum contains two main peaks of $2p_{3/2}$ and $2p_{1/2}$ with the energy gap of 11.6 eV corresponding to Mn^{4+}, which has been described in many previous reports.[23] There is a shoulder at around 637.8 eV related to the Auger peak. Satellite peaks indicate the presence of minor surface Mn^{3+} stemming from the minor extraction of surface Na, occurring in many layered oxides.[24] In the Fe 2p spectrum, the two main peaks at 711.8 and 725.3 eV correspond to $2p_{3/2}$ and $2p_{1/2}$, respectively. The spectrum shows satellite peaks and reveals an oxidation state of +3 for Fe.[17,25] Overall, the XPS results confirm that the oxidation states of Mn and Fe for the pristine $Na_{0.8}Li_{0.2}Fe_{0.2}Mn_{0.6}O_2$ material are +4 and +3, respectively. These values are expected for achieving a complete charge balance in the compound assuming O (−2) and Na/Li (+1).

High resolution transmission electron microscopy (HRTEM) and selected area electron diffraction (SAED) were used to study the local, nanoscopic properties of the sample. From HRTEM, the shape of most crystallites looks plate-like indicating preferred orientation of the (00ℓ) planes (ℓ=2 for P2 and ℓ=3 for O3 materials). **Figure 2**a,c shows two different particles and the areas selected for SAED analysis. The small particles surrounding the large particles are the minor fraction of the sample relating to a C/2m phase and/or sodium carbonates and sodium hydroxides. Figure 2b and d show the SAED patterns corresponding to Figure 2a,c. **Figure 3**b clearly indicates an O3 structure. More SAED patterns of the same particle are shown in Figure S3, Supporting Information. All of them show the typical O3 phase pattern. In contrast to this, the results for the other particle shown in Figure 2d, indicate a P2 structure. There are also some other signals, however, marked with arrows. To clarify their origin, Fast Fourier Transformation (FFT, Figure 2e,f) was performed from a selected area. P2 (red circles) and O3 (cyan squares) models match well with the FFT image, which demonstrates the coexistence of P2 and O3 structures. Inverse Fast Fourier Transformation (IFFT) was applied to study the distribution of P and O phase within the crystallite (Figure 2g,h). It is clearly observed that both phases are distributed within the particle. We also studied more particles and found the same property. Nevertheless, the presence of larger amounts of defects makes it challengeable to clearly differentiate between structures, such as stacking faults, superstructures or grain boundaries, as shown in Figures S3, S4, and S5, Supporting Information. Overall, XRD and TEM analysis provide clear evidence for a biphasic nature of the material that shows also an intimate P2/O3 mixture within individual crystals.

The lattice positions of the alkali metals were investigated by ssNMR. ^{23}Na and ^{6}Li NMR spectra are shown in Figure 3a,b. The ^{23}Na solid state NMR spectrum of $Na_{0.8}Li_{0.2}Fe_{0.2}Mn_{0.6}O_2$ is characterized by the presence of three main signals centered at around 2200, 1700, and −20 ppm together with the MAS rotational sidebands marked by "*". The chemical shift range of a ^{23}Na nuclei in a diamagnetic compound is normally in the range of 60 to −50 ppm, for example, sodium carbonates, sodium hydroxide. Strong deviations from these shifts are usually observed in the NMR spectra of Na-containing paramagnetic compounds (as in the case of $Na_{0.8}Li_{0.2}Fe_{0.2}Mn_{0.6}O_2$). The magnitude and sign of such paramagnetic shifts is approximately determined by the sum of the individual Na-O-TM paramagnetic interactions at each particular crystallographic sodium site.[26] It has been observed previously that ^{23}Na NMR resonances of octahedral coordinated sites in layered oxide materials are affected by stronger paramagnetic shifts as

© 2020 The Authors. Published by Wiley-VCH GmbH

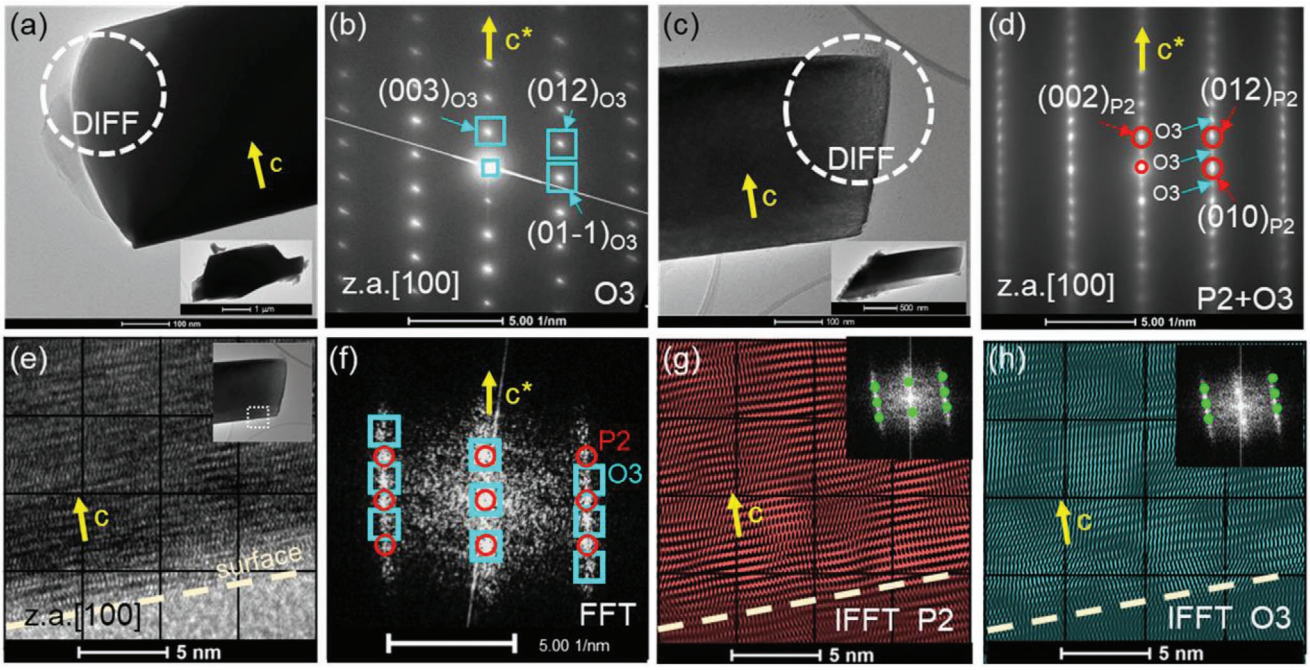

Figure 2. TEM images, SAED patterns, FFT, and filtered IFFT images of $Na_{0.8}Li_{0.2}Ni_{0.2}Mn_{0.6}O_2$. TEM images of single O3 (a) and biphasic P2/O3 particle (c). The insert image shows the corresponding complete particle. The circles indicate the areas from which SAED patterns where recorded, see (b) showing single phase O3 and (d) showing a biphasic P2/O3 structure (a more detailed discussion is provided in the main text). (e) and (f) show the HRTEM and FFT image of the P2/O3 biphasic particle. The insert image shows the surveyed area. Cyan squares and red circles are corresponding to O3 and P2 phase, respectively. IFFT images of P2 phase (g) and O3 phase (h) obtained by the corresponding insert P2 and O3 FFT patterns.

compared to the P2 counterparts, due to the shorter distances between the Na ions and the paramagnetic TM centers in the octahedral coordination as well as by the angular orientations of the orbitals involved in the paramagnetic interactions.[12b,27] Also, prismatically coordinated Na ions in P2 phases are normally characterized by narrower resonances due to the fast Na

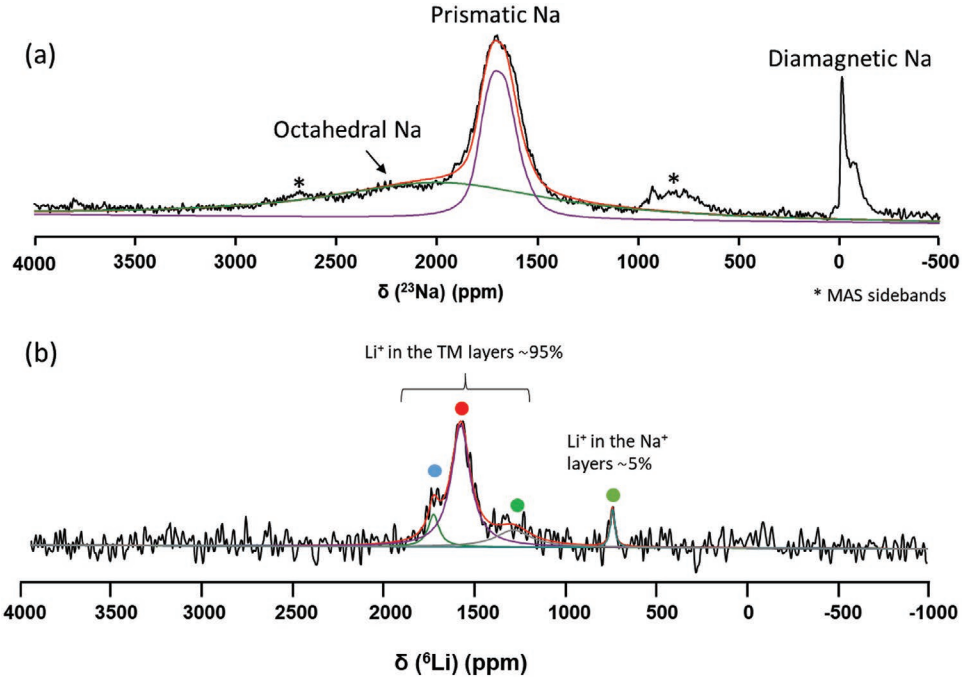

Figure 3. Magic angle spinning (MAS) solid state NMR spectra of ^{23}Na (a) and ^{6}Li (b) for $Na_{0.8}Li_{0.2}Fe_{0.2}Mn_{0.6}O_2$. Asterisk (*) represent MAS rotational sidebands. The plus sign (+) represents resonance of diamagnetic species. The group of signals marked with blue, red and green spots assigned to Li ions at TM layers close to Fe and/or Mn, whereas the light green dot indicates Li in Na layers.

© 2020 The Authors. Published by Wiley-VCH GmbH

ion diffusion in the 2D layers of the compounds.[12b,19,28] This effect is not observed in the octahedrally coordinated materials due to the restricted motions of the Na ion this case. From all the previous considerations, it is quite straightforward to assign the broad component centered at around 2200 ppm to Na ions in the O3 type structure of the material, the signal at 1700 ppm to the P2 coordinated Na sites and the narrower signal close to 0 ppm to a diamagnetic secondary phase. These diamagnetic impurities (such as sodium carbonate) are commonly observed in layered oxides.[13b,29] Note that the quantity of the $C2/m$ secondary phase visible by XRD is too small to be detectable by ssNMR. The narrower character of the P2 signal is in agreement with previous observations, where the presence of fast Na ion motions in the 2D layers of P2 compounds can effectively reduce the magnitude of the dipolar paramagnetic interaction reducing the resulting NMR linewidths.[27] This observation, therefore, further corroborates the assignment made for the signals in Figure 3a. A good fitting (red curve) is obtained assuming the phase fractions obtained from XRD. Note that an independent fitting of the NMR signals was not feasible due to their broadness. The fitting of the P2 signal in the figure was obtained considering a quadrupolar nature of the ^{23}Na NMR resonance. The presence of quadrupolar features for this signal agrees with a rather homogeneous environment for Na ions located at the prismatic sites.

Further $^{6/7}$Li solid state NMR spectra were performed for $Na_{0.8}Li_{0.2}Fe_{0.2}Mn_{0.6}O_2$. ^{7}Li isotope is normally selected for NMR experiments, as it has a higher gyromagnetic ratio compared with ^{6}Li isotope. However, polarization of paramagnetic ^{7}Li, which is caused by dipolar interactions between nuclei and unpaired electrons, leads to an extended pattern of MAS sidebands that can be a problem due to the strong overlapping of the signals and the difficulties in the correct signal deconvolution and assignment. However, this can be suppressed in ^{6}Li NMR spectra, as dipolar interactions in this case are very much reduced and the MAS rotational sidebands can be avoided at the fast MAS frequencies used in this case of 50 kHz.[19] Considering this, we only show the ^{6}Li ssNMR spectra here (Figure 3b). This spectrum is characterized by a main group of signals centered at around 1560 ppm and a narrow signal of lower intensity at 750 ppm. These values coincide very well with the shifts for Li ions at the TM layers (1700–1400 ppm) and Li ions at the octahedral sites of the P2 alkali planes (500–800 ppm) reported previously for Ni–Mn[7] and Fe–Mn[19] systems. This assignment is based on the observation of stronger paramagnetic shifts of the ^{6}Li NMR signals of Li ions at the TM planes, as in this case the Li-TM interactions are expected to be stronger.

Quantification of the data reveals an estimated 95% of total Li content in the TM layers whereas it is only 5% for Li in the alkali layer. However, it is challenging to distinguish lithium from the P2 or O3 phase. This is because lithium in the TM layers has the same octahedral coordination in both phases, and the amount of lithium in alkali layer is too little to analyze which phase they located. The spectra were further deconvoluted to determine the various positions of the Li ions. The signals with maxima at around 1750 ppm (blue dot), 1600 ppm (red dot), and 1400 ppm (green dot) correspond to Li in the metal oxide layer close to Fe, Mn, and Li, respectively.[15a,19] The Li peak intensity at 1600 ppm is highest indicating Li preferentially located close to Mn.

2.2. Electrochemical Properties

The electrochemical properties of $Na_{0.8}Li_{0.2}Fe_{0.2}Mn_{0.6}O_2$ were characterized by galvanostatic charge/discharge experiments in half cells with Na-metal as counter electrode between 2.0–4.6 V (versus Na^+/Na). 4.6 V was chosen as upper cut-off to study structural changes over a wide compositional range. The higher the cut-off, the more likely risk for electrolyte oxidation which, however, was not a severe issue in our measurements. Moreover, positive electrodes may be charged to higher potentials without electrolyte oxidation due to thermodynamic reasons.[30] **Figure 4**a shows charge-discharge profiles for selected cycles (1st to 100th cycle) at a rate of C/10 (0.1 C=15 mA g^{-1}). The first cycle is notably different from the later ones indicating an activation of the material that is commonly observed for many layered oxides.[5a,14a,29b,31] During 1st charging, the voltage increases gradually up to 4.0 V. Above 4.3 V, the curve flattens and a weak distinct plateau appears which may be originated from oxygen redox behavior as previously reported for Li-substituted layered oxides.[14a,22] The material exhibits an initial reversible capacity of 174 mAh g^{-1}, corresponding to a change in Na content of $x = 0.62$ per formula unit (the theoretical capacity being 225 mAh g^{-1} for $x = 0.8$).

During second charging, the voltage raises sharply until 3.5 V. After reaching this point, the behavior is comparable to the first charging. Figure 4b,c shows the average discharge/charge voltage and the stability over 100 cycles. Some general characteristics of the electrode reaction can be revealed from the electrochemical studies:

1. The overall reversibility is high. Starting from 174 mAh g^{-1}, the capacity reaches 146 mAh g^{-1} after 100 cycles (C/10). This corresponds to a capacity retention of 82%. This leads to an energy round trip efficiency slightly above 80%, see Figure S6. Its initial coulombic efficiency is relatively low, due to the decomposition of the $C2/m$ phase during the initial charging. However, an average coulombic efficiency of 98% is reached in the following cycles.
2. The electrode reaction in this voltage window includes, $Fe^{3+/4+}$, partial $Mn^{3+/4+}$ as well as oxygen redox, which is also confirmed by the XAS in the following section.[11,32] The contribution of the oxygen redox plateau becomes weaker over cycling, and the overall shapes of the discharge/charge curves become sloping.
3. The voltage profiles change over cycling. The charging voltage decreases, especially during the first ten cycles (see Figure 4a,b). This voltage fade of a few hundred mV is also observed in Li-rich layered oxides[33] and has been attributed to transition metal ion migration and trapping.[34] Similar to our material, these types of materials also contain excess lithium ions in the TM layers. The discharging voltage also slightly decreases upon cycling but the effect is less pronounced compared to the charging process. This slight change might be caused by the slight loss of the long-range order and the ions migration (Fe and Li) during cycling. Starting from 2.92 V, the average voltage drops to 2.66 V after

© 2020 The Authors. Published by Wiley-VCH GmbH

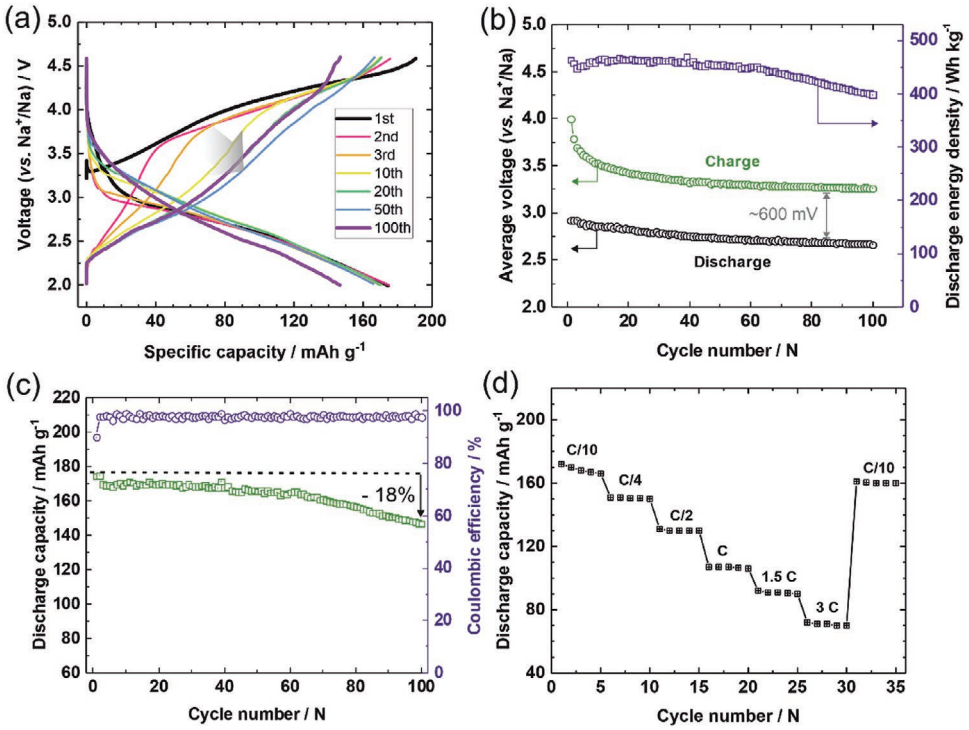

Figure 4. a) Galvanostatic charge-discharge profiles for selected cycles (1st to 100th cycle) of the $Na_{0.8}Li_{0.2}Fe_{0.2}Mn_{0.6}O_2$ electrode between 2.0–4.6 V at C/10. The arrow indicates the voltage fade during cyling; b) average charge/discharge voltage and discharge energy density over 100 cycles at rate of C/10; c) capacity retention and coulombic efficiency and d) rate capability test (1C=150 mA g^{-1}). All cells were cycled in two-electrode cells with sodium as counter electrode.

100 cycles, corresponding to a retention of 91%. Changes in the voltage profiles may be also understood from very recent results by House et al., who linked a voltage drop to loss of a superstructure (though this was only studied for the first cycle).[22] The average voltage gap between charging and discharging stabilizes over cycling and amounts to about 600 mV at C/10. The corresponding energy density of the reaction (spec. capacity × av. discharge voltage) is between 400–460 Wh kg^{-1} during the cycling.

2.3. Structural Changes upon Cycling

While many electrochemical studies on the cycle life of sodium layered oxides are published, the knowledge on structural changes upon cycling is often poor due to the complexity of the reaction. In the following, we try to shed more lights on the reaction of the present material using XAS, XRD, and ssNMR.

Ex situ XAS was conducted to explore the changes in valence state and local environment in an element selective way. **Figure 5** shows the Fe and Mn K-edge X-ray absorption near edge structure (XANES) and extended X-ray absorption fine structure (EXAFS) of $Na_{0.8}Li_{0.2}Fe_{0.2}Mn_{0.6}O_2$ before cycling (pri), fully charged (FC) state at 4.6 V and its fully discharged (FD) state at 2.0 V. The edge position of the Fe K-edge spectrum (Figure 5a) of the pristine sample is similar to that of the Fe_2O_3 standard, indicating the initial Fe oxidation state of Fe^{3+}, which well agrees with the XPS result. As the Na ions are deintercalated, the shape of Fe K-edge spectra changes, but there is not a rigid shift to higher energy. Although the origin of the spectral shape changes at Fe K-edge XANES is not clearly understood yet, the same trend has been linked to oxidation of Fe^{3+} during Na deintercalation.[11,35] Upon subsequent discharging to 2.0 V, the shape of Fe K-edge absorption returns, suggesting that the Fe oxidation state returns to 3+. EXAFS results on the (average) Fe-O inter atomic distance changes further support the Fe redox, see Figure 5b. The average Fe-O distance in the pristine material is around 1.56 Å. When the electrode is fully charged to 4.6 V, the distance decreases to 1.41 Å, indicating oxidation of Fe^{3+} to higher oxidation states. Note that the R values of the peaks are about 0.3–0.5 Å shorter than the actual bond length because the FT-EXAFS spectrum were not phase corrected. The Fe–O distance increases again during discharging reaching 1.53 Å at 2.0 V. The Fe–M distance undergoes a slight shift from 2.55 to 2.52 Å upon Na extraction and returns to its initial state after recharging. The insert enlarged graph for the Fe pre-edge region shows an increase in intensity after charging. Subsequent discharging, however, only leads to a slight reduction of the pre-edge peak, which indicates irreversible Fe migration from octahedral to sodium sites, similar as reported for $NaFeO_2$[36] and $Na_{2/3}Ni_{1/6}Mn_{1/2}Fe_{1/3}O_2$.[37] This irreversible Fe migration contributes to the polarizations we observed in electrochemical results. Overall, the results suggest a reversible change of the Fe oxidation states during charging/discharging between Fe^{3+} and Fe^{4+}.

For the Mn K-edge XANES, MnO_2 and Mn_2O_3 were chosen as the reference for Mn^{4+} and Mn^{3+}, respectively, as shown Figure 5c. For the pristine material, the Mn K-edge energy

© 2020 The Authors. Published by Wiley-VCH GmbH

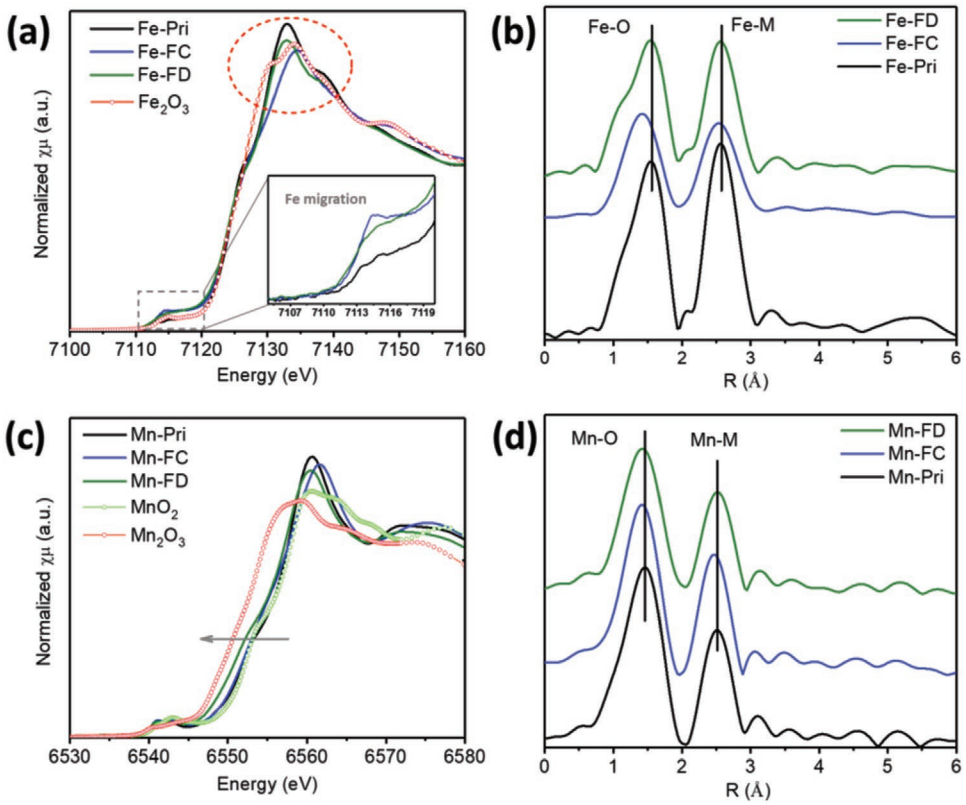

Figure 5. Fe (a) and Mn (c) K-edge XANES and EXAFS spectra of Fe (b) and Mn (d) of $Na_{0.8}Li_{0.2}Fe_{0.2}Mn_{0.6}O_2$ for selected states: Before cycling (Pri), fully charged (FC@4.6 V), and fully discharged (FD@2.0 V) within the initial cycle (M=Mn, Fe, Li). The insert graph shows the enlarged pre-edge region of Fe. The data indicates migration of Fe ions from the transition metal layer to the alkali layer.

is close to the edge position of MnO_2 reference suggesting that the initial oxidation state of Mn is 4+ (in line with XPS results). The signal is remained after charging to 4.5 V, while after subsequent discharging to 2.0 V, the Mn K-edge energy slightly shifted to lower energy. This is consistent with the electrochemical measurement. This indicates partial reduction of Mn^{4+} to Mn^{3+} during discharging. The Mn–O (Figure 5d) distance decreases upon charging to 1.41 Å and then remains at this value, even after subsequent discharging. This is likely linked to the activation of the electrode in the first cycle as also seen from the electrochemical results. It is worth mentioning that the change in atomic distances of TM-M (TM=Fe, Mn, M=transition metals and Li) is as reversible as that of Fe-O. Again, this might be caused by oxygen redox processes occurring in the high voltage region as discussed above and also further below using ssNMR.

In principle, A-O-A (A=alkali elements) bonds can support the formation of new π-bonding and antibonding molecular orbitals which are responsible for the oxygen reduction.[38] In order to further prove oxygen redox activity in this material, XAS oxygen K-edge spectrum was measured using partial fluorescence yield mode (PFY), as shown in **Figure 6**. Two peaks can be found at around 529.3 and 531.5 eV, corresponding to the transition of O 1s electrons to the unoccupied O 2p orbitals hybridized with TM 3d, in line with other published results.[39] However, an additional broad but notable absorption peak appears at higher energy region (marked with dash circle) after charging because the oxygen oxidation raises the nuclear charge as well as the 1s-2p hybridization energy. This new absorption peak after charging has been observed in O K-edge spectra of other materials such as Na_2RuO_3,[40] $Na_{0.6}Li_{0.2}Mn_{0.8}O_2$ [27], and $Na_{2/3}Mg_{0.28}Mn_{0.72}O_2$.[32,41] The peak shifted to 529 eV and

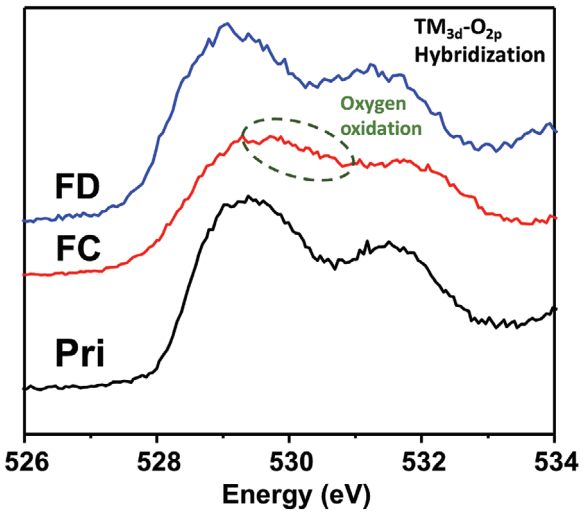

Figure 6. X-ray absorption spectra for O K-edge with selected range from 526–534 eV for the pristine material (Pri, black), after full charging (FC@4.6 V, red) and after full discharging (FD@2.0 V, blue).

© 2020 The Authors. Published by Wiley-VCH GmbH

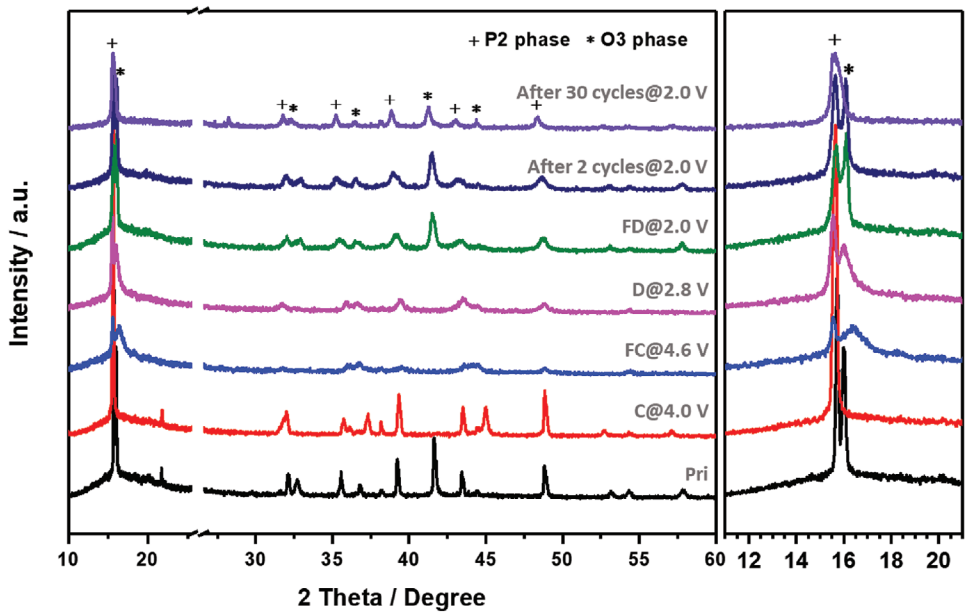

Figure 7. XRD patterns of $Na_{0.8}Li_{0.2}Fe_{0.2}Mn_{0.6}O_2$ at selected states of before cycling (Pri), charged 4.0 V (C@4.0 V), initially charged 4.6 V (FC@4.6 V) and initially discharged 2.8 V (D@2.8 V), after one cycle (FD@2.8 V), two cycles (@2.0 V) and 30 cycles (@2.0 V). The plus sign (+) and asterisk (*) marked the reflexes of P2 and O3 phase, respectively. The curve on the right shows the intensity and position changes of the (00*l*) reflex (*l*=2 for P2 phase, *l*=3 for O3 phase).

presented a little broadening, being a hint on reversible oxygen redox activity within the initial cycle of the material.

Results from XRD are shown in **Figure 7**. The reflex from the Al current collector between $2\theta = 25.6°–26.6°$ was removed for better clarity. Reflexes of the P2 and O3 phase are marked with plus sign (+) and asterisk (*), respectively. The non-cycled electrode shows the same structure as the pristine powder, indicating stability of the compound during electrode preparation. Note that many sodium layered oxides are moisture sensitive which is why we conducted the complete electrode preparation in the glove box.[42]

After charging to 4.0 V (C@4.0 V), the reflexes centered at $2\theta = 16.0°$, 32.7°, 37.2°, and 41.6° have vanished, indicating disappearance of the O3 phase. This has not been observed for this type of P/O biphasic materials yet. When further charged to 4.6 V (FC@4.6 V), all reflexes become weaker, that is, there is a general loss in long-range order. A new reflex appearing at 16.3° indicates the reappearance of a new O (O2 or O1) phase at high voltage, which is ascribed to the rearrangement of the oxygen array.[7] Of note, the reflexes of the *C*2/*m* secondary phase at 22° disappear at this stage. The disappearance of this phase might contribute to the initial irreversible capacity. Overall, the XRD results at different states of charging indicate that the reaction involves several consecutive phase transitions (O→P→O) with an overall decrease in structural order.

During discharging, the reflexes are all maintained as the fully charged state when discharged to 2.8 V (D@2.8 V). After completely first discharged to 2.0 V (FD@2.0 V), also the O3-reflexes (see 28.6° and 16.1°) become again stronger revealing that after one cycle, the biphasic composition is reformed. The same structure is also obtained after the second cycle. All reflexes can also be observed even after 30 cycles. Overall, the electrode undergoes reversible phase transitions during charging and discharging. It is clear that further studies are required to understand the complete phase behavior during cycling, however, we consider the reversible formation of the biphasic structure as an important reason for the observed good cycling stability.

^{23}Na and $^{6/7}$Li solid state NMR experiments were conducted in order to determine the positions of the alkali ions and their coordination after electrochemical cycling. Measurements were performed for samples after fully charge state (FC@4.6 V) and fully discharged state of first (FD@2.0 V) and tenth cycle (2.0 V). The ^{7}Li NMR spectra of these samples are displayed in **Figure 8**a together with the ^{6}Li NMR spectrum of the pristine material for reference. As discussed before, ^{7}Li NMR spectra are normally characterized by broader resonances with a manifold of rotational sidebands whereas ^{6}Li NMR experiments are generally better resolved.[43] Unfortunately, ^{6}Li NMR experiments were not feasible in our ex situ materials as the active materials are significantly diluted in this case aggravating the low sensitivity of this low abundant isotope. We can nevertheless characterize the Li occupancies in the alkali and TM layers using the ^{7}Li NMR spectra taking the red reference experiment for the pristine material as a reference (grey and pink boxes respectively). Looking to Figure 8a, it is evident that the relative populations of Li at the alkali and TM layers are changing when the cell is charged to 4.6 V. At this stage, a significant Li population that was initially at the TM layers has migrated to the alkali layers in order to compensate the low Na^+ population. From inspection of the spectra obtained after the first (FD@2.0 V) and tenth cycle (2.0 V), we can clearly conclude that this migration is not reversible upon sodium reintroduction and that the Li occupancies remain constant during the consequent cycles.

The ^{23}Na ssNMR spectra of the cycled samples are shown in Figure 8b and compared to the pristine material. As stated

© 2020 The Authors. Published by Wiley-VCH GmbH

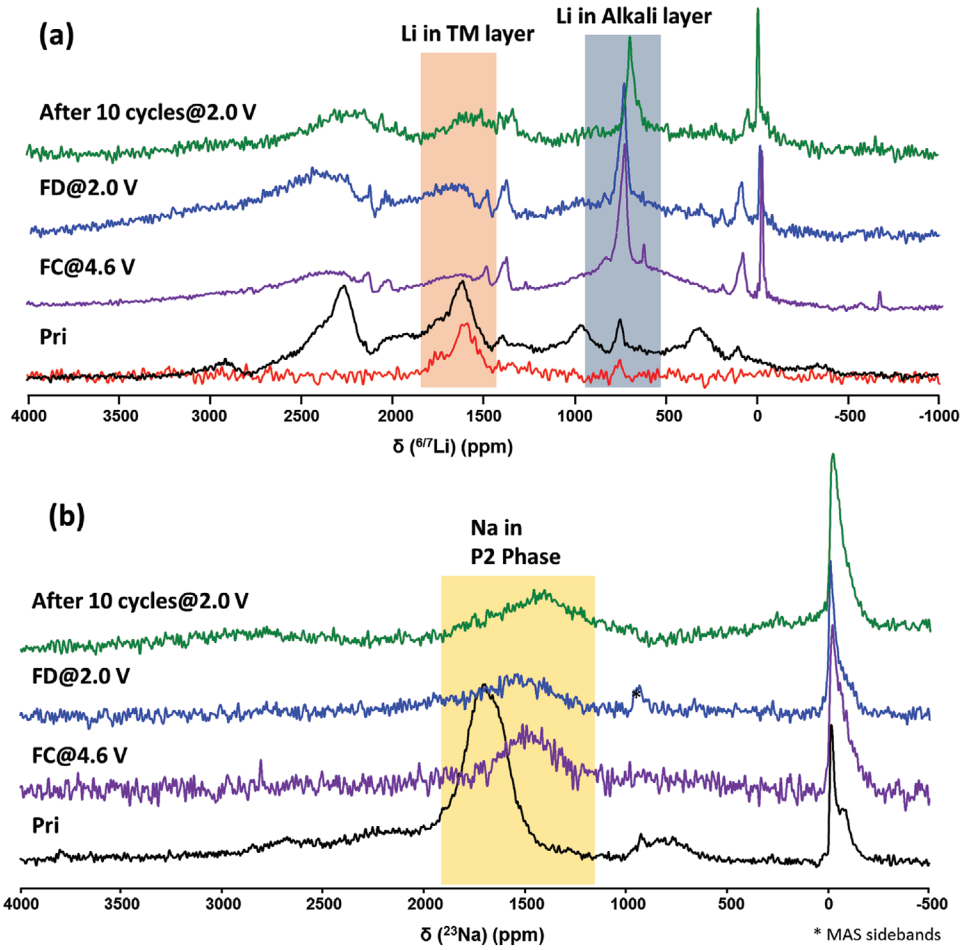

Figure 8. ssNMR study on (a) $Li^7$and (b) Na^{23} for $Na_{0.8}Li_{0.2}Fe_{0.2}Mn_{0.6}O_2$ at different stages (pristine, FC@4.6 V, FD@2.0 V, after ten cycles@2.0 V). The^{6}Li and ^{7}Li NMR spectra of pristine material are shown in red and black in the figure. The real signals are marked as "+". The yellow shadows highlight the Na signal from Na in P2 phase. The orange and blue shadows highlight the Li resonances corresponding to TM layer and alkali layer, respectively. Only ^{7}Li NMR spectra were recorded for ex situ samples, due to the very low intensity of the low abundant ^{6}Li isotopes, their low polarization and the lower effective mass that is loaded in the MAS rotors in ex situ samples, as these are also mixed with super C65 carbon and PVDF.

above, the signals close to 0 ppm stem from sodium containing diamagnetic compounds such as sodium carbonates and remains from the electrolyte salt. After charging, that is, after desodiation, a weak signal remains which has shifted to a lower paramagnetic value of around 1500 ppm. This shift is in agreement with an overall oxidation of the TM centers, as the average number of unpaired electrons in the TM layer is reduced and therefore the paramagnetic impact in the NMR spectrum.[29b,44] The presence of a measurable ^{23}Na NMR signal at 4.6 V indicates the presence of minor amounts of sodium irreversibly trapped (or not electrochemically active in the measured voltage window). The XRD analysis performed for this material confirmed the biphasic P2/O3 nature of the pristine state (see previous section), in agreement with the NMR results discussed in Figure 3a.

It is well known that layered oxide materials at concentrations of alkali ions (in the alkali layers) close to saturation preferentially lead to O-type structures. From the analysis of the ^{7}Li NMR spectra of Figure 8a, we could conclude that there is a partial Li migration from the TM layers to the alkali layers after the first discharge and that this Li population remains at the alkali layers in the consequent electrochemical cycles. The ^{23}Na signal of the O3 components is not observable but this can be understood from signal broadening. ^{23}Na ssNMR of octahedrally coordinated ions in O-type layered oxides containing Fe and Mn are generally strongly shifted to higher ppm values and subject of strong broadening due to the absence of fast ion diffusion in the 2D alkali layers.[12b,27] This signal broadening can be further increased if the material presents a rather heterogeneous character rendering their ^{23}Na NMR resonances undistinguishable from the baseline in the NMR spectrum. This increase in structural heterogeneity is evidenced by broadening of the remaining P2 signal of the cycled samples as compared to the pristine material. We therefore assign the absence of the octahedrally coordinated Na ions in Figure 8b to this signal broadening effects.

3. Conclusion

A sodium layered oxide with the overall stoichiometry $Na_{0.8}Li_{0.2}Fe_{0.2}Mn_{0.6}O_2$ was synthesized by sol-gel method

© 2020 The Authors. Published by Wiley-VCH GmbH

followed by calcination. The material is Co- and Ni-free and contains lithium as structure stabilizer. It shows a biphasic P2/O3 structure with relative amounts of both phases of 34% for P2 and 60% for O3, respectively. A minor secondary phase was detected as well. This material contains two types of crystals, O3-single crystals and P2/O3 biphasic crystals. The oxidation states of iron and manganese in the pristine material are (+3) and (+4), respectively. Moreover, 95% of the lithium was found to be located in the TM layer while only 5% in the alkali layer.

The electrode delivered an initial capacity of 174 mAh g^{-1} and showed a capacity retention of 82% over 100 cycles. The charging voltage curve showed a voltage fade, especially within the first 20 cycles indicative for some restructuring/ordering as well as the Fe migration from the octahedral site to the sodium site in the material. Analysis of electrodes at different charge/discharge states revealed that complex phase transitions take place with the O phase being the dominant fraction after several cycles. Despite the phase transitions and a general loss in long-range order (decrease of XRD reflex intensities), the biphasic nature of the material is preserved at fully discharged state (2.0 V) even after 30 cycles. The redox activity of the electrode is dominated by Fe with partial Mn and O contributions. ssNMR results indicated that Li ions are distributed between the TM and the alkali layers in the pristine material, although some Li migration from the TM to the alkali layers occurred within the first charge. This new redistribution of the lithium remained constant during subsequent electrochemical cycling (the cycled ten times electrode was detected). As a consequence of such redistribution, the alkali concentration at the alkali layers of the material is close to saturation in the cycled samples (2.0 V) inducing a larger proportion of octahedrally coordinated O3-structures. Broadening of the solid state NMR signals could also show some structural heterogeneity of the compound after cycling. Lithium predominantly remains in the TM layer during cycling supporting the idea that lithium acts as stabilizer. Needless to say that further improvements are required but considering the fact that the material is free of Co and Ni, the overall performance is good and supports the idea that layered oxides composed of mixed P/O phase may be an attractive route for improving the performance of cathode materials for SIBs.

Supporting Information

Supporting Information is available from the Wiley Online Library or from the author.

Acknowledgements

P.A. and T.R. thank for support within the LIBRA project funded over the EIG Concert Japan program financed by BMBF (01DR18003), MINECO (PCI2018-093068), and JST. L.Y. thanks the China Scholarship Council for funding. The authors acknowledge Ms. S. Stumpf for the SEM images from the SEM facilities of the Jena Center for Soft Matter (JCSM) established with a grant from the German Research Council (DFG) and the European Funds for Regional Development (EFRE). The support by R. Wagner and M. Schürmann for XPS from Chair of material science is also gratefully acknowledged. Z.S., S.-M.B., and X.-Q.Y. at Brookhaven National Laboratory were supported by the U.S. Department of Energy, the Assistant Secretary for Energy Efficiency and Renewable Energy, Office of Vehicle Technologies through Advanced Battery Material Research (BMR) program under Contract No. DE-SC0012704. This research used resources at beamlines 7-BM (QAS) and 23-ID-2 (IOS) of the National Synchrotron Light Source II, a U.S. Department of Energy (DOE) Office of Science User Facility operated for the DOE Office of Science by Brookhaven National Laboratory under Contract No. DE-SC0012704.

Conflict of Interest

The authors declare no conflict of interest.

Author Contributions

L.Y., P.N., and P.A. conceived the idea, L.Y. and P.N. synthesized the material, performed XRD and all electrochemical measurements, J.B. did Rietveld refinement studies and results were discussed with M.G., TEM studies were done by F.B., NMR studies were done by J.M.A. and L.Y., XAS measurements were done by Z.S., S.-M. B., and X.-Q. Y. The data and manuscript were organized by L.Y. The manuscript was written by L.Y. and P.A. and was edited by all authors. All authors contributed to the discussion.

Keywords

energy storage, layered oxides, positive electrode materials, sodium ion batteries

Received: April 16, 2020
Revised: June 19, 2020
Published online: August 21, 2020

[1] a) M. S. Whittingham, *Chem. Rev.* **2004**, *104*, 4271; b) M. Armand, J. M. Tarascon, *Nat. Mater.* **2001**, *414*, 359; c) P. K. Nayak, E. M. Erickson, F. Schipper, T. R. Penki, N. Munichandraiah, P. Adelhelm, H. Sclar, F. Amalraj, B. Markovsky, D. Aurbach, *Adv. Energy Mater.* **2018**, *8*, 1702397.
[2] a) W. Liu, M. S. Song, B. Kong, Y. Cui, *Adv. Energy Mater.* **2017**, 29; b) P. Adelhelm, *Angew. Chem., Int. Ed.* **2018**, *57*, 6710.
[3] a) L. Middlemiss, A. Holland, *Squarespace* **2018**, *1*, 1; b) J. W. Choi, D. Aurbach, *Nat. Rev. Mater.* **2016**, *1*, 16013.
[4] a) P. K. Nayak, L. Yang, W. Brehm, P. Adelhelm, *Angew. Chem., Int. Ed.* **2018**, *57*, 102; b) C. Vaalma, D. Buchholz, M. Weil, S. Passerini, *Nat. Mater.* **2018**, *3*, 1.
[5] a) M. H. Han, E. Gonzalo, G. Singh, T. Rojo, *Energy Environ. Sci.* **2015**, *8*, 81; b) K. Kubota, S. Kumakura, Y. Yoda, K. Kuroki, S. Komaba, *Adv. Energy Mater.* **2018**, *8*, 1703415.
[6] C. Delmas, C. Fouassier, P. Hagenmuller, *Physics B&C* **1980**, *99B*, 81.
[7] R. J. Clément, P. G. Bruce, C. P. Grey, *J. Electrochem. Soc.* **2015**, *162*, A2589.
[8] L. Yang, Y. Xia, L. Qin, G. Yuan, B. Qiu, J. Shi, Z. Liu, *J. Power Sources* **2016**, *304*, 293.
[9] J. Billaud, G. Singh, A. R. Armstrong, E. Gonzalo, V. Roddatis, M. Armand, T. Rojo, P. G. Bruce, *Energy Environ. Sci.* **2014**, *7*, 1387.
[10] a) A. Bhandari, J. Bhattacharya, *J. Electrochem. Soc.* **2017**, *164*, A106; b) N. Ortiz-Vitoriano, N. E. Drewett, E. Gonzalo, T. Rojo, *Energy Environ. Sci.* **2017**, *10*, 1051.

© 2020 The Authors. Published by Wiley-VCH GmbH

[11] N. Yabuuchi, M. Kajiyama, J. Iwatate, H. Nishikawa, S. Hitomi, R. Okuyama, R. Usui, Y. Yamada, S. Komaba, *Nat. Mater.* **2012**, *11*, 512.
[12] a) W. M. Dose, N. Sharma, J. C. Pramudita, H. E. A. Brand, E. Gonzalo, T. Rojo, *Chem. Mater.* **2017**, *29*, 7416; b) E. Gonzalo, M. H. Han, J. M. López del Amo, B. Acebedo, M. Casas-Cabanas, T. Rojo, *J. Mater. Chem. A* **2014**, *2*, 18523.
[13] a) E. Talaie, V. Duffort, H. L. Smith, B. Fultz, L. F. Nazar, *Energy Environ. Sci.* **2015**, *8*, 2512; b) R. J. Clément, J. Billaud, A. Robert Armstrong, G. Singh, T. Rojo, P. G. Bruce, C. P. Grey, *Energy Environ. Sci.* **2016**, *9*, 3240.
[14] a) E. de la Llave, E. Talaie, E. Levi, P. K. Nayak, M. Dixit, P. T. Rao, P. Hartmann, F. Chesneau, D. T. Major, M. Greenstein, D. Aurbach, L. F. Nazar, *Chem. Mater.* **2016**, *28*, 9064; b) X. Rong, J. Liu, E. Hu, Y. Liu, Y. Wang, J. Wu, X. Yu, K. Page, Y.-S. Hu, W. Yang, H. Li, X.-Q. Yang, L. Chen, X. Huang, *Joule* **2018**, *2*, 125.
[15] a) J. Xu, D. H. Lee, R. J. Clément, X. Yu, M. Leskes, A. J. Pell, G. Pintacuda, X.-Q. Yang, C. P. Grey, Y. S. Meng, *Chem. Mater.* **2014**, *26*, 1260; b) J. Xu, H. Liu, Y. S. Meng, *Electrochem. Commun.* **2015**, *60*, 13; c) H. Liu, J. Xu, C. Ma, Y. S. Meng, *Chem Commun (Camb)* **2015**, *51*, 4693.
[16] L. Yang, X. Li, J. Liu, S. Xiong, X. Ma, P. Liu, J. Bai, W. Xu, Y. Tang, Y.-Y. Hu, M. Liu, H. Chen, *J. Am. Chem. Soc.* **2019**, *141*, 6680.
[17] S. Guo, P. Liu, H. Yu, Y. Zhu, M. Chen, M. Ishida, H. Zhou, *Angew. Chem., Int. Ed.* **2015**, *54*, 5894.
[18] M. Keller, D. Buchholz, S. Passerini, *Adv. Energy Mater.* **2016**, *6*, 1501555.
[19] M. Bianchini, E. Gonzalo, N. E. Drewett, N. Ortiz-Vitoriano, J. M. López del Amo, F. J. Bonilla, B. Acebedo, T. Rojo, *J. Mater. Chem. A* **2018**, *6*, 3552.
[20] G. K. Veerasubramani, Y. Subramanian, M.-S. Park, B. Senthilkumar, A. Eftekhari, S. J. Kim, D.-W. Kim, *Electrochim. Acta* **2019**, *296*, 1027.
[21] B. Mortemard de Boisse, D. Carlier, M. Guignard, C. Delmas, *J. Electrochem. Soc.* **2013**, https://doi.org/10.1149/2.032304jes]A569.
[22] R. House, U. Maitra, M. Perez-Osario, J. Lozano, L. Jin, J. Somerville, M. Roberts, P. Bruce, *Nature* **2020**, *577*, 502.
[23] a) S. Hussain, R. Amade, E. Jover, E. Bertran, *ScientificWorldJournal* **2013**, *2013*, 832581; b) H. W. Nesbitt, D. Banerjee, *Am. Mineral.* **1998**, *83*, 305; c) A. Ramírez, P. Hillebrand, D. Stellmach, M. M. May, P. Bogdanoff, S. Fiechter, *J. Phys. Chem. C* **2014**, *118*, 14073.
[24] a) L. Wang, Y.-G. Sun, L.-L. Hu, J.-Y. Piao, J. Guo, A. Manthiram, J. Ma, A.-M. Cao, *J. Mater. Chem. A* **2017**, *5*, 8752; b) S. Mariyappan, Q. Wang, J. M. Tarascon, *J. Electrochem. Soc.* **2018**, *165*, A3714.
[25] L. R. Merte, J. Gustafson, M. Shipilin, C. Zhang, E. Lundgren, *Catalysis, Structure & Reactivity* **2017**, *3*, 95.
[26] D. S. Middlemiss, A. J. Ilott, R. J. Clément, F. C. Strobridge, C. P. Grey, *Chem. Mater.* **2013**, *25*, 1723.
[27] G. Singh, B. Acebedo, M. C. Cabanas, D. Shanmukaraj, M. Armand, T. Rojo, *Electrochem. Commun.* **2013**, *37*, 61.
[28] a) R. J. Clément, J. Xu, D. S. Middlemiss, J. Alvarado, C. Ma, Y. S. Meng, C. P. Grey, *J. Mater. Chem. A* **2017**, *5*, 4129; b) G. Singh, N. Tapia-Ruiz, J. M. Lopez del Amo, U. Maitra, J. W. Somerville, A. R. Armstrong, J. Martinez de Ilarduya, T. Rojo, P. G. Bruce, *Chem. Mater.* **2016**, *28*, 5087.
[29] a) M. Kalapsazova, S. Ivanova, R. Kukeva, S. Simova, S. Wegner, E. Zhecheva, R. Stoyanova, *Physical Chemistry Chemical Physics: PCCP* **2017**, *19*, 27065; b) G. Singh, J. M. López del Amo, M. Galceran, S. Pérez-Villar, T. Rojo, *J. Mater. Chem. A* **2015**, *3*, 6954.
[30] P. K. Nayak, L. Yang, W. Brehm, P. Adelhelm, *Angew. Chem.* **2018**, *57*, 102.
[31] B. Song, E. Hu, J. Liu, Y. Zhang, X.-Q. Yang, J. Nanda, A. Huq, K. Page, *J. Mater. Chem. A* **2019**, *7*, 1491.
[32] U. Maitra, R. A. House, J. W. Somerville, N. Tapia-Ruiz, J. G. Lozano, N. Guerrini, R. Hao, K. Luo, L. Jin, M. A. Perez-Osorio, F. Massel, D. M. Pickup, S. Ramos, X. Lu, D. E. McNally, A. V. Chadwick, F. Giustino, T. Schmitt, L. C. Duda, M. R. Roberts, P. G. Bruce, *Nat. Chem.* **2018**, *10*, 288.
[33] P. Rozier, J. M. Tarascon, *J. Electrochem. Soc.* **2015**, *162*, A2490.
[34] M. Sathiya, A. M. Abakumov, D. Foix, G. Rousse, K. Ramesha, M. Saubanere, M. L. Doublet, H. Vezin, C. P. Laisa, A. S. Prakash, D. Gonbeau, G. VanTendeloo, J. M. Tarascon, *Nat. Mater.* **2015**, *14*, 230.
[35] J. Zhao, J. Xu, D. H. Lee, N. Dimov, Y. S. Meng, S. Okada, *J. Power Sources* **2014**, *264*, 235.
[36] a) N. Yabuuchi, S. Komaba, *Sci. Technol. Adv. Mater.* **2014**, *15*, 043501; b) N. Yabuuchi, H. Yoshida, S. Komaba, *Electrochemistry* **2012**, *80*, 716.
[37] J. W. Somerville, A. Sobkowiak, N. Tapia-Ruiz, J. Billaud, J. G. Lozano, R. A. House, L. C. Gallington, T. Ericsson, L. Häggström, M. R. Roberts, U. Maitra, P. G. Bruce, *Energy Environ. Sci.* **2019**, *12*, 2223.
[38] R. A. House, U. Maitra, L. Jin, J. G. Lozano, J. W. Somerville, N. H. Rees, A. J. Naylor, L. C. Duda, F. Massel, A. V. Chadwick, S. Ramos, D. M. Pickup, D. E. McNally, X. Lu, T. Schmitt, M. R. Roberts, P. G. Bruce, *Chem. Mater.* **2019**, *31*, 3293.
[39] a) B. Mortemard de Boisse, S.-i. Nishimura, E. Watanabe, L. Lander, A. Tsuchimoto, J. Kikkawa, E. Kobayashi, D. Asakura, M. Okubo, A. Yamada, *Adv. Energy Mater.* **2018**, *8*, 1800409; b) M. Okubo, A. Yamada, *ACS Appl. Mater. Interfaces* **2017**, *9*, 36463.
[40] N. Yabuuchi, M. Nakayama, M. Takeuchi, S. Komaba, Y. Hashimoto, T. Mukai, H. Shiiba, K. Sato, Y. Kobayashi, A. Nakao, M. Yonemura, K. Yamanaka, K. Mitsuhara, T. Ohta, *Nat. Commun.* **2016**, *7*, 13814.
[41] a) C. Ma, J. Alvarado, J. Xu, R. J. Clément, M. Kodur, W. Tong, C. P. Grey, Y. S. Meng, *J. Am. Chem. Soc.* **2017**, *139*, 4835; b) C. Zhao, Q. Wang, Y. Lu, Y.-S. Hu, B. Li, L. Chen, *J. Phys. D: Appl. Phys.* **2017**, *50*, 183001.
[42] a) L. Zheng, J. Li, M. N. Obrovac, *Chem. Mater.* **2017**, *29*, 1623; b) M. H. Han, N. Sharma, E. Gonzalo, J. C. Pramudita, H. E. A. Brand, J. M. López del Amo, T. Rojo, *J. Mater. Chem. A* **2016**, *4*, 18963.
[43] C. P. Grey, N. Dupré, *Chem. Rev.* **2004**, *104*, 4493.
[44] J. Martinez De Ilarduya, L. Otaegui, J. M. López del Amo, M. Armand, G. Singh, *J. Power Sources* **2017**, *337*, 197.

© 2020 The Authors. Published by Wiley-VCH GmbH